ORIGINAL ARTICLE

Abyssal current and water mass in the Main Gap and an adjacent Small Gap of the Emperor Seamount Chain

Daigo Yanagimoto[1] · Masatoshi Miyamoto[2] · Eitarou Oka[1] · Toshiya Nakano[3] · Yasushi Takatsuki[4] · Hiroyuki Tsujino[5]

Abstract

From 2016 to 2017, we conducted 1-year mooring current observation at the widest, deepest gap, widely known as the Main Gap, and a narrower, shallower gap just south of the Main Gap, called the Small Gap in this study, in the Emperor Seamount Chain, which divides the Northwest Pacific Basin (NWPB) from the Northeast Pacific Basin. We also conducted two hydrographic sections with a conductivity–temperature–depth sensor and a lowered acoustic Doppler current profiler around the two gaps in 2012 and 2016. At the Main Gap, the abyssal current flowed east–northeastward at a statistically significant mean velocity of 1.3–2.4 cm s^{-1}, while the current was dominated by tidal and inertial variability with a magnitude of 3–4 cm s^{-1}. At the Small Gap, the abyssal current had an eastward mean velocity of 9.4 cm s^{-1}, accompanied by mesoscale variability with a magnitude of 7 cm s^{-1}. These eastward currents carried abyssal water below a depth of 5000 m, which came from the northern part of the NWPB, with a volume transport of 1.6×10^6 m^3 s^{-1} through the Main Gap and 0.5×10^6 m^3 s^{-1} through the Small Gap. Cold, saline, oxygen-rich Lower Circumpolar Deep Water, which occupied the south of the zonal seamount range at 37°N, called the S–E Seamounts in this study, was found near the seafloor north of the S–E Seamounts to the west of the Small Gap; however, it did not extend to the Main Gap or to the east of the Small Gap.

1 Introduction

The global deep ocean circulation brings cold, saline, oxygen-rich Lower Circumpolar Deep Water (LCDW) below a depth of 3500 m from the Southern Ocean to the world oceans. It plays an important role in transporting heat and materials as the lowest portion of the global meridional overturning circulation (Richardson 2008). Deep western boundary currents (DWBCs) are the major transporter of LCDW in the deep ocean circulation, while deep mesoscale variability has also been recently suggested to have some contribution to the transport of deep waters (Bower et al. 2009, 2011; Miyamoto et al. 2017, 2020).

In the Pacific Ocean, the DWBC enters the Central Pacific Basin through the Samoan Passage carrying LCDW from the south (Fig. 1; Mantyla and Reid 1983; Rudnick 1997). It then bifurcates into a shallower western branch and a deeper eastern branch, due to the sill depth of approximately 4500 m between the Central Pacific Basin and the Melanesian Basin (Johnson and Toole 1993; Kawabe et al. 2003). While a part of the eastern branch separates eastward and enters the Northeast Pacific Basin (NEPB) (Kato and Kawabe 2009), the rest of it enters the southern part of the Northwest Pacific Basin (NWPB) through the Wake Island Passage (Kawabe et al. 2005). Because there is a sill with depth of approximately 5150 m along 37°N between the Shatsky Rise and the Emperor Seamount Chain (ESC), the

✉ Daigo Yanagimoto
daigo@aori.u-tokyo.ac.jp

1. Atmosphere and Ocean Research Institute, The University of Tokyo, 5-1-5, Kashiwanoha, Kashiwa 277-8564, Japan

2. Osaka Regional Headquarters, Japan Meteorological Agency, 4-1-76, Otemae, Chuo, Osaka 540-0008, Japan

3. Atmosphere and Ocean Department, Japan Meteorological Agency, 3-6-9, Toranomon, Minato, Tokyo 105-8431, Japan

4. Meteorological College, Japan Meteorological Agency, 7-4-81, Asahicho, Kashiwa 277-0852, Japan

5. Meteorological Research Institute, Japan Meteorological Agency, 1-1, Nagamine, Tsukuba 305-0052, Japan

Fig. 1 Pathway of deep ocean circulation in the western Pacific. The thick arrow shows the main route of the deep ocean circulation transporting the largest volume of LCDW, and thin arrows show its bifurcations (Kawabe and Fujio 2010). The broken line from the Kuril Trench to the Aleutian Trench and dotted lines at the Main Gap show unsolved routes from the Northwest Pacific Basin to the Northeast Pacific Basin. The bottom topography is based on the ETOPO1 1 Arc-minute Global Relief Model of the NOAA National Geophysical Data Center, which was downloaded from https://doi.org/10.7289/V5C8276M
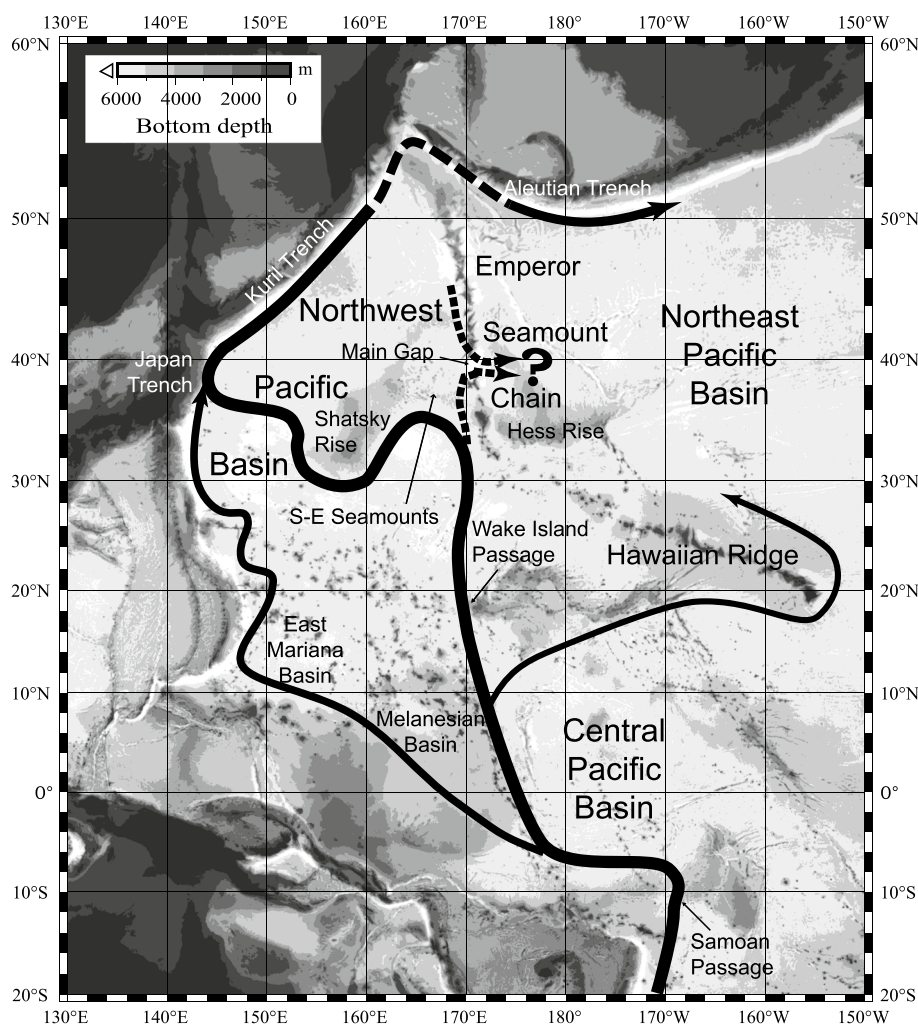
eastern branch makes an anticlockwise turn south of the sill (Yanagimoto and Kawabe 2007); this sill is called the S–E Seamount in this study. Then, the eastern branch turns clockwise south of the Shatsky Rise (Yanagimoto et al. 2010), joins the western branch to the east of the Japan Trench (Fujio and Yanagimoto 2005), and advances further northward (Ando et al. 2013). Finally, it is believed to flow out from the NWPB to the NEPB (Owens and Warren 2001; Kawabe and Fujio 2010).

The NWPB and the NEPB are separated by the ESC, which ranges meridionally for approximately 2400 km along ~170°E between the Aleutian Trench and the Hawaiian Ridge. The ESC consists of tall and steep guyots rising up to 20–2000 m below the sea surface and crests standing at about 3000–5000 m above the ocean floor (Roden et al. 1982) affecting the shallow flow field at depths less than 2000 m (Wagawa et al. 2012). Moreover, the ESC acts as a barrier for the deep ocean circulation in the two basins. Besides the junction of the Kuril Trench and the Aleutian Trench that is believed to be the most plausible route from the NWPB to the NEPB (broken line in Fig. 1), several gaps

in the ESC can be pathways for the deep water (Owens and Warren 2001). Among them, the widest, deepest gap with an approximately 100-km width and 6000-m depth, called the Main Gap, is thought to be the most important pathway.

Owens and Warren (2001) illustrated an eastward current through the Main Gap on their schematic of deep currents in the western North Pacific based on historical studies, including a 17-month mooring observation that detected a strong northeastward flow over the steep slope at the southernmost part of the Main Gap (Hamann and Taft 1987), although they left it unresolved whether the eastward current comes from the north or south (dotted arrows in Fig. 1). Komaki and Kawabe (2009) demonstrated an eastward abyssal flow transporting relatively oxygen-rich and cold water at the center of the Main Gap based on shipboard conductivity–temperature–depth (CTD) profiler and lowered acoustic Doppler profiler (LADCP) observations, speculating that a part of the LCDW separating from the eastern branch and crossing over the S–E Seamounts might pass the Main Gap. Nevertheless, observations around the Main Gap are still very few and fragmentary.

This study focuses on two major questions indicated by a question mark in Fig. 1, that is, whether the abyssal water is carried eastward through the Main Gap on average, and where the abyssal water comes from. To answer these questions, we intensively observed abyssal currents around the Main Gap from 2016 to 2017. In addition, we surveyed deep currents in a small gap just south of the Main Gap for an alternate pathway of deep water across the ESC.

2 Observation and data

2.1 Mooring observations

The KH-16–3 cruise of the R/V *Hakuho Maru* was carried out in June 2016 (Fig. 2a; Oka et al. 2020). The vessel departed from Tokyo on 31 May, arrived at the ESC area on 9 June, left there on 13 June, and returned to Tokyo on 29 June. Our study area is shown by a broken-line rectangle in Fig. 2a and is enlarged in Fig. 2b. The study area is located to the east of the Shatsky Rise, containing four tall named guyots of the ESC standing in a row: the Nintoku, Jingu, Ojin and Koko Guyots. The Jingu and Ojin Guyots are two peaks of one massive seamount, surrounded by a single isobath of 3000 m. There is a nameless guyot to the north of Koko Guyot, called K–N Guyot hereafter. The Main Gap lies between the Nintoku and Ojin Guyots. Between the K–N and Ojin Guyots lies a small gap of the ESC, called the Small Gap in this study. The Small Gap is a narrow passage with a width of about 30 km and is a low sill with a depth of approximately 5200 m (Fig. 2c). To the west of the K–N Guyot, small seamounts extend zonally along approximately 37°N to the Shatsky Rise (Fig. 2b). We call them the S–E Seamounts hereafter. The S–E Seamounts have a sill depth of approximately 5150 m, preventing the deeper portion of LCDW from passing northward (Yanagimoto and Kawabe 2007).

We deployed two mooring systems ME1 and ME2 in the Main Gap and one mooring system ME3 in the Small Gap on 10, 11, and 12 June 2016, respectively (Fig. 2b). To avoid the effect of steep topography, ME1 and ME2 were moored over the flat seafloor in the Main Gap. ME3 was located near the center of the Small Gap to avoid the steep slopes of the guyots (Fig. 2c). We successfully recovered ME3 and ME1 in the second leg of the C40 cruise of Hokkaido University's T/V *Oshoro Maru* on 24 and 25 June 2017, respectively. However, our effort to recover ME2 during the cruise resulted in failure, perhaps due to troubles in the acoustic releaser.

At ME1, we moored four current meters at depths of 4045, 5045, 5445, and 5845 m above the seafloor at 5895 m; the upper three were 3D-ACMs, which were single-point current meters manufactured by Falmouth Scientific, Inc.,

and the lowest is a downward-looking 300-kHz Workhorse Sentinel, which was an ADCP manufactured by Teledyne RD Instruments. At ME3, two 3D-ACMs and one downward-looking 300-kHz Workhorse Sentinel were moored at depths of 4160, 4760, and 5163 m, respectively, on the seafloor at 5213 m (determined by a ship-mounted precision depth recorder). Both at ME1 and ME3, ADCP records from the vertical cells at 4-m intervals were similar to one another except for the cells near the mooring releasers (~20 m below the instruments), where measured velocities were small probably due to the reflection of the pings (not shown). We adopted ADCP data from the second cell which was 10 m below the instruments. Unfortunately, we failed in accessing records in the two upper instruments at ME1 and the uppermost one at ME3 due to memory trouble. Furthermore, the second upper instrument at ME3 failed in reconstructing current vectors from three-dimensional measurements along instrument coordinates. Overall, we obtained three data sets at 5445 m (ME1–3) and 5855 m (ME1–4) of ME1, and at 5173 m (ME3–3) of ME3 (Table 1).

All the current meters were set to record current velocity components every hour. We call them hourly current in this study. We subsampled them every midnight Coordinated Universal Time after filtering out inertial oscillations and diurnal and semi-diurnal tides using a Gaussian filter called gaus24 (Thompson 1983). We call them daily current hereafter.

2.2 CTD/LADCP observations and hydrographic data sets

Fifteen full-depth CTD casts from the surface to approximately 10 m above the seafloor were conducted around the Main Gap and the Small Gap during the KH-16–3 cruise (stations H01 to H15 in Fig. 2b and Table 2). Two LADCPs (300-kHz Workhorse Monitor) were attached at the top and bottom of the CTD frame with its transducer turned upward and downward, respectively. We obtained absolute current velocity profiles from these LADCPs within the depth range, where bottom-track velocity was available by downward-looking LADCP (below approximately 100 m above the seafloor). To remove noise, we averaged them between 10 and 50 m above the seafloor.

The Japan Meteorological Agency (JMA) operated the RF1206 cruise of R/V *Ryofu Maru* in July to September 2012 (Fig. 2a) and conducted full-depth CTD/LADCP observations around the Main Gap (R01 to R27 in Fig. 2b and Table 2). We reproduced vertical profiles of LADCP current data by the same method as for KH-16–3. Unlike the KH-16–3 observation, only a downward-looking LADCP was set on the CTD frame.

The CTD data of the KH-16–3 and RF1206 sections in Table 2 were used to identify the abyssal water at the Main
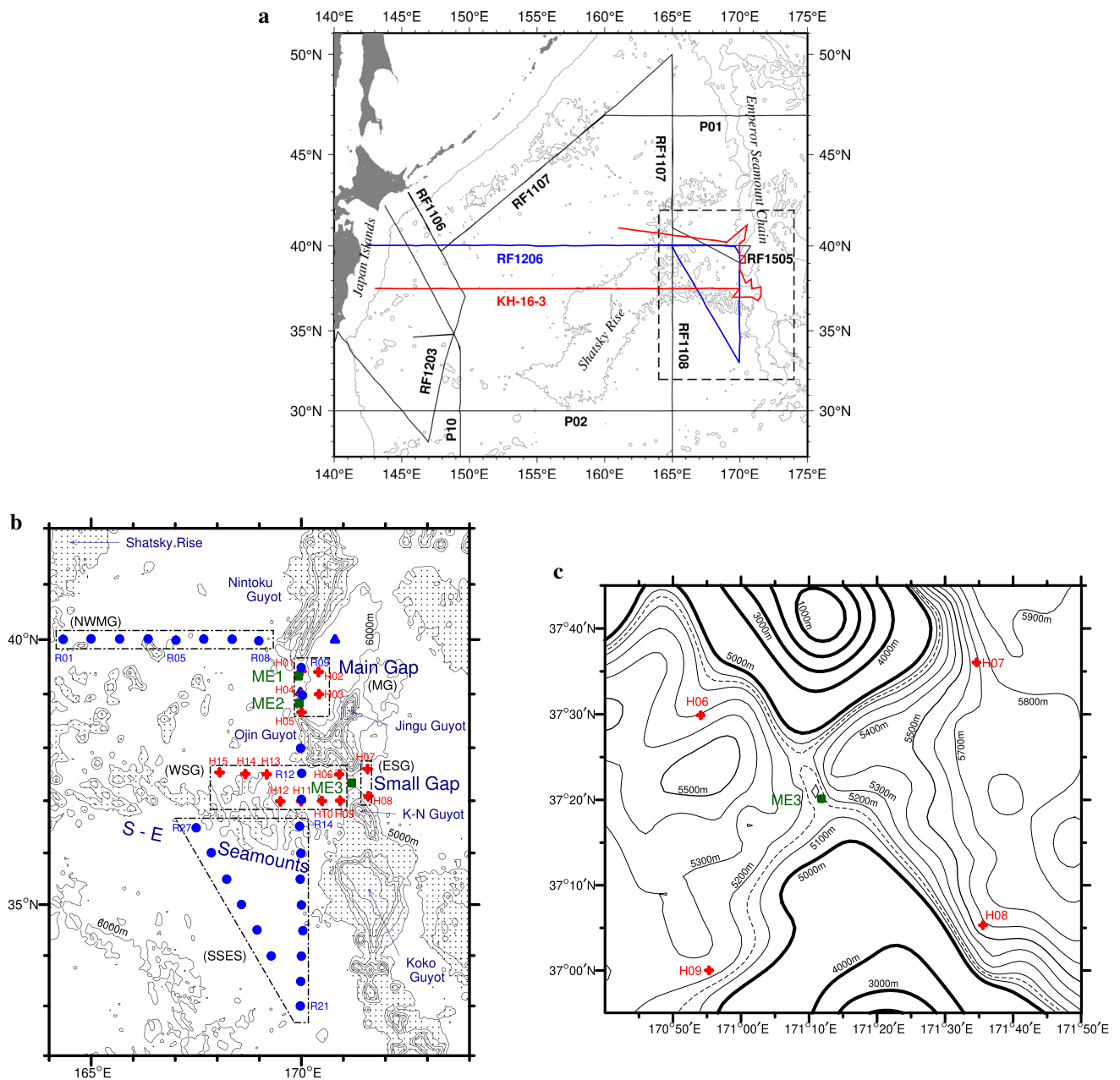
Fig. 2 Location of the observations in this study. **a** Observation lines of the KH-16–3 cruise by R/V *Hakuho Maru* (red line), RF1206 cruise by R/V *Ryofu Maru* (blue line), and other hydrographic sections used in this study (black line) in the northwest Pacific. Thin black lines denote 5000-m isobaths. The dashed black line denotes the region of our mooring and CTD/LADCP observations, which is enlarged in (**b**). **b** Positions of moorings and full-depth CTD/LADCP sites around the Main Gap and the Small Gap. The mooring systems ME1–ME3 are shown by green boxes. Full-depth CTD/LADCP stations H01–H15 in KH-16–3 and R01–R27 in RF1206 are shown by blue circles and red crosses, respectively. These stations are classified into five geographical regions whose names have been placed in parentheses (see text). Two blue triangles are CTD stations of RF1505. Solid lines are isobaths of every 1000 m, and hatched areas are shallower than a 5000-m depth. **c** Further enlarged view of bottom topography around the Small Gap. Thick solid lines are isobaths of every 1000 m from a 5000-m depth; thin solid lines are those of every 100 m from 5000-m to 6000-m depths, and thin broken lines are those of a 5150-m depth. Topography in all maps is based on ETOPO1

Gap and the Small Gap. To compare water properties among the gaps and their surrounding areas, we classified our CTD/LADCP stations into five geographic regions: NWMG, MG, WSG, ESG and SSES (Fig. 2b). The NWMG region is located along 40°N between the Shatsky Rise and the ESC, the MG region is in the Main Gap, the WSG region is to the west of the Small Gap, and the ESG region is to the east of the Small Gap. The SSES region, to which LCDW is carried

Table 1 Moored instruments recovered successfully and statistics of eastward and northward velocity components (u, v) of their daily current (smoothed as in text)

Data ID	Depth [m]	Record length [days]	Average [cm s^{-1}] with standard error		Integral time scale [days]	
			$\bar{u} \pm \varepsilon_u$	$\bar{v} \pm \varepsilon_v$	τ_u	τ_v
ME1 39°20.06′N, 169°55.98′E, 5895-m bottom depth						
FSI 3D-ACM current meter at 5445-m depth						
ME1–3	5445	380	2.1 ± 0.6	1.2 ± 1.4	7.2	21.2
TRDI Workhorse 300 kHz ADCP at 5845-m depth						
ME1–4	5855	380	1.1 ± 0.3	0.6 ± 0.9	3.3	17.9
ME3 37°20.13′N, 171°11.84′E, 5213-m bottom depth						
TRDI Workhorse 300 kHz ADCP at 5163-m depth						
ME3–3	5173	377	9.2 ± 1.9	-1.7 ± 0.6	11.7	11.4

We used current records from the second cell of Workhorse ADCP as ME1–4 and ME3–3

directly from the south (Yanagimoto and Kawabe 2007), is located to the south of S–E Seamounts.

We also investigated a wider distribution of water properties using recent full-depth hydrographic data sets from the following sections or cruises; P01 in 2014, P02 in 2013, and P10 in 2012 archived by the CLIVAR and Carbon Hydrographic Data Office (CCHDO), and RF1106, RF1107 and RF1108 in 2011, RF1203 in 2012, and RF1505 in 2015 operated by the JMA's R/V *Ryofu Maru* (Fig. 2a). Hydrographic data around the Main Gap were enriched by two casts at 39°59.76′N, 170°48.02′E and 39°01.73′N, 169°58.49′E in the RF1505 cruise (blue triangles in Fig. 2b). We also used hydrographic data of the RF1206 cruise besides those listed in Table 2. Data sets from CCHDO and JMA were downloaded from https://cchdo.ucsd.edu/ and https://www.data.jma.go.jp/gmd/kaiyou/db/vessel_obs/data-report/html/ship/ship_e.php, respectively.

All of the full-depth CTD data used in this study were obtained down to approximately 10 m above the seafloor and were calibrated with water sampling measurements by data managers of each cruise. In addition, we corrected the calibrated CTD salinity data, adding the batch-to-batch offsets of the International Association for the Physical Sciences of the Oceans (IAPSO) Standard Seawater (SSW) evaluated by Uchida et al. (2020): + 0.0004 for the batch P153 used in P02, P10, RF1106, RF1107, RF1108, and RF1203, + 0.0005 for P154 in RF1206, + 0.0004 for P156 in P01 and RF1505, and -0.0004 for P159 in KH-16–3.

3 Abyssal current

3.1 Temporal characteristics of currents observed by moorings

Time series of daily current vectors at the mooring systems ME1 and ME3 are shown by stick diagrams in Fig. 3. The histograms of daily current direction are plotted with solid lines in Fig. 4. The eastward current was dominant at both moorings; the positive (eastward) velocity component accounted for a percentage of 73%, 74%, and 85% at ME1–3, ME1–4, and ME3–3, respectively.

At ME1, daily time-series at both depths resembled each other. Coherences between the two depths were sufficiently high over confidence limits at all frequencies both for eastward (u) and northward (v) velocity components (not shown). The average velocities at both depths directed to the east–northeast, although they were small (1.3 cm s^{-1} toward 66°T at ME1–4 and 2.4 cm s^{-1} toward 60°T at ME1–3; Fig. 3). The standard errors estimated as $\sigma/(2\,T/\tau)^{-1}$, where σ, T, τ are standard deviation, record length, and integral time scale, respectively (Dickson et al. 1985), were so small for the u component that the averages of u were statistically significant (Table 1). Furthermore, we can also see the dominance of positive u also in hourly current velocity, which contains various time-scale variabilities from tides and inertial oscillation to several-month-scale variabilities; the eastward hourly currents occurred with a frequency of 61 to 65%, as shown by the broken lines in Fig. 4. On the other hand, the averages of v were small, within the standard errors at both depths.

The eastward current at ME3 was stable and strong through the observation period, except for periods during June to July 2016, September 2016, and December 2016 to January 2017 (Fig. 3). Its average velocity was 9.4 cm s^{-1} toward 100°T. Both u and v had sufficiently larger averages than standard errors (Table 1). The mean current vector even exceeded the standard deviation ellipse (Fig. 3).

The time scale of current variability was examined using variances of hourly u and v in three period bands of T > 20 days, 20 > T > 2 days, and T < 2 days, where T is the period in days (Fig. 5). Bands of T > 20 and T < 2 represent mesoscale variability and tidal and inertial variability, respectively. At ME1–3 and ME1–4, the T < 2 band had the largest distribution equivalent to current speed of 3–4 cm s^{-1}. The T < 2 band at ME3–3 also had an equivalent

Table 2 Full-depth CTD/LADCP stations carried out in this study

Station number	Original stn. number	Latitude	Longitude	Seafloor depth [m]	Reaching-bottom time (UTC)
R/V *Hakuho Maru* KH-16–3 cruise					
H01	C014	39°25.08′N	170°00.27′E	5842	10 Jun. 2016, 10:34
H02	C015	39°24.49′N	170°24.56′E	6236	10 Jun. 2016, 16:23
H03	C016	38°59.81′N	170°25.13′E	6339	10 Jun. 2016, 23:10
H04	C017	38°59.55′N	170°00.44′E	5860	11 Jun. 2016, 07:54
H05	C018	38°39.88′N	170°00.34′E	6261	11 Jun. 2016, 13:44
H06	C021	37°29.89′N	170°54.08′E	5183	12 Jun. 2016, 08:55
H07	C022	37°36.05′N	171°34.00′E	5659	12 Jun. 2016, 16:06
H08	C023	37°05.32′N	171°35.56′E	5622	13 Jun. 2016, 01:46
H09	C025	37°00.02′N	170°55.30′E	5284	13 Jun. 2016, 11:25
H10	C026	36°59.71′N	170°29.63′E	5280	13 Jun. 2016, 16:52
H11	C027	36°59.53′N	169°59.65′E	5201	13 Jun. 2016, 22:14
H12	C028	36°59.33′N	169°29.85′E	5145	14 Jun. 2016, 03:47
H13	C030	37°29.99′N	169°10.48′E	5248	14 Jun. 2016, 18:48
H14	C032	37°30.48′N	168°40.04′E	5210	15 Jun. 2016, 04:48
H15	C33B	37°32.26′N	168°03.35′E	5199	16 Jun. 2016, 05:37
R/V *Ryofu Maru* RF1206 cruise					
R01	RF4503	40°00.29′N	164°20.07′E	5333	10 Aug. 2012, 22:43
R02	RF4502	40°00.88′N	164°59.83′E	5582	10 Aug. 2012, 15:32
R03	RF4501	40°00.75′N	165°40.62′E	5553	10 Aug. 2012, 07:35
R04	RF4500	40°00.77′N	166°21.27′E	5504	09 Aug. 2012, 23:43
R05	RF4499	39°59.39′N	167°00.98′E	6001	09 Aug. 2012, 14:26
R06	RF4504	40°00.58′N	167°40.70′E	5815	25 Aug. 2012, 04:10
R07	RF4505	40°00.39′N	168°21.18′E	5851	25 Aug. 2012, 13:55
R08	RF4507	39°58.64′N	168°59.30′E	6008	27 Aug. 2012, 19:37
R09	RF4509	39°29.27′N	169°59.80′E	5917	28 Aug. 2012, 09:44
R10	RF4510	38°58.61′N	170°01.62′E	6077	28 Aug. 2012, 16:55
R11	RF4512	37°59.41′N	169°58.98′E	4804	29 Aug. 2012, 08:34
R12	RF4513	37°31.18′N	170°00.47′E	5415	29 Aug. 2012, 15:06
R13	RF4514	37°01.50′N	169°59.99′E	5314	29 Aug. 2012, 22:43
R14	RF4515	36°30.70′N	169°57.52′E	4536	30 Aug. 2012, 05:55
R15	RF4516	35°59.50′N	169°59.26′E	5325	30 Aug. 2012, 12:49
R16	RF4517	35°29.64′N	169°58.38′E	5516	30 Aug. 2012, 19:43
R17	RF4518	34°59.50′N	170°00.06′E	5598	31 Aug. 2012, 02:35
R18	RF4519	34°29.33′N	170°02.11′E	5531	31 Aug. 2012, 09:23
R19	RF4520	33°59.33′N	169°59.95′E	5754	31 Aug. 2012, 16:12
R20	RF4521	33°29.35′N	169°59.09′E	5842	31 Aug. 2012, 23:15
R21	RF4522	33°00.03′N	169°58.52′E	5843	01 Sep. 2012, 06:39
R22	RF4523	33°59.55′N	169°16.96′E	5682	01 Sep. 2012, 16:24
R23	RF4524	34°30.31′N	168°56.76′E	5705	01 Sep. 2012, 23:47
R24	RF4525	35°00.12′N	168°34.54′E	5711	02 Sep. 2012, 07:17
R25	RF4526	35°29.61′N	168°13.44′E	5713	02 Sep. 2012,14:44
R26	RF4527	36°00.30′N	167°51.49′E	5551	02 Sep. 2012, 22:05
R27	RF4528	36°28.99′N	167°29.88′E	5718	03 Sep. 2012, 05:41

current speed of about 4 cm s^{-1}. Thus, tidal and inertial variability was dominant at the Main Gap and was equivalent to 3–4 cm s^{-1} at both the Main Gap and the Small Gap. Incidentally, T > 20 band was the smallest among u components; this is the cause of the short integral time scale and extremely small standard error for u at ME1 (Table 1). On the other hand, the u component of T > 20 band at ME3–3 had the largest value equivalent to a current speed of about 7 cm s^{-1}. Mesoscale variability was dominant at the Small Gap; its kinetic energy of 27.2 cm^2 s^{-2} was approximately
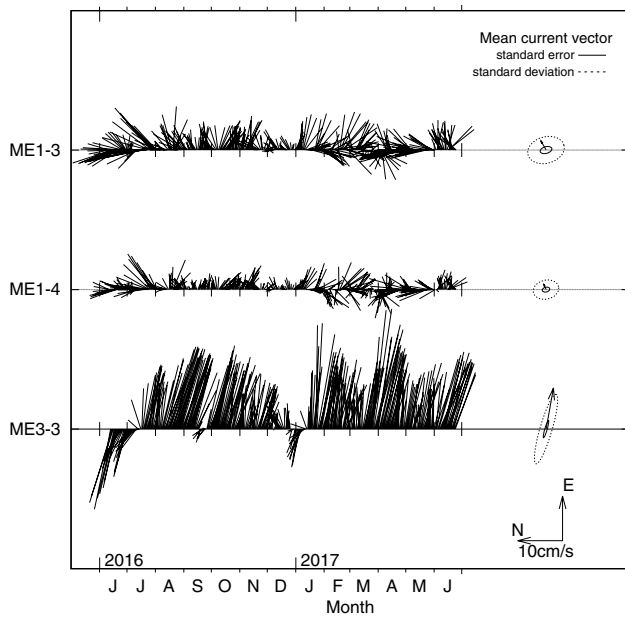
Fig. 3 Stick diagrams and statistics of daily current vectors at ME1–3, ME1–4, and ME3–3. Statistics are shown by the same scale as the stick diagrams on the right side; mean currents are shown by arrows, and standard errors and deviations are shown by solid-line and broken-line ellipses, respectively

five times larger than that of 5.4 cm² s⁻² at most at the Main Gap (mesoscale kinetic energy was calculated as a half of the summation of the variances of u and v for T > 20 band shown in Fig. 5).

3.2 Horizontal distribution of currents

We next examined the horizontal distribution of LADCP current vectors averaged between 10 and 50 m from the seafloor in comparison with the record-length mean current vectors by the moored instruments (Fig. 6). Though snapshot measurements by LADCP cannot reveal mean currents, they are helpful for examining the horizontal expanse of current variability. Weak currents equivalent to or smaller than the T < 2-day band variability detected at ME1 existed at H01–H04, R09 and R10 around ME1. In addition, current directions were scattered at H01–H04 on the same day (Table 2). These results are consistent with the dominance of the tidal and inertial fluctuations at ME1.

Compared to the currents in the Main Gap, the LADCP currents around and to the west of the Small Gap seemed to have coherent structures with a horizontal scale of several tens to one hundred kilometers. Relatively strong westward to northwestward currents existed around ME3: 5.5 cm s⁻¹ (335°T) at H09, 6.8 cm s⁻¹ (265°T) at H08, and 9.4 cm s⁻¹ (288°T) at H06. These were measured on 12 and 13 June 2016, which were the first 2 days of the period that ME3–3
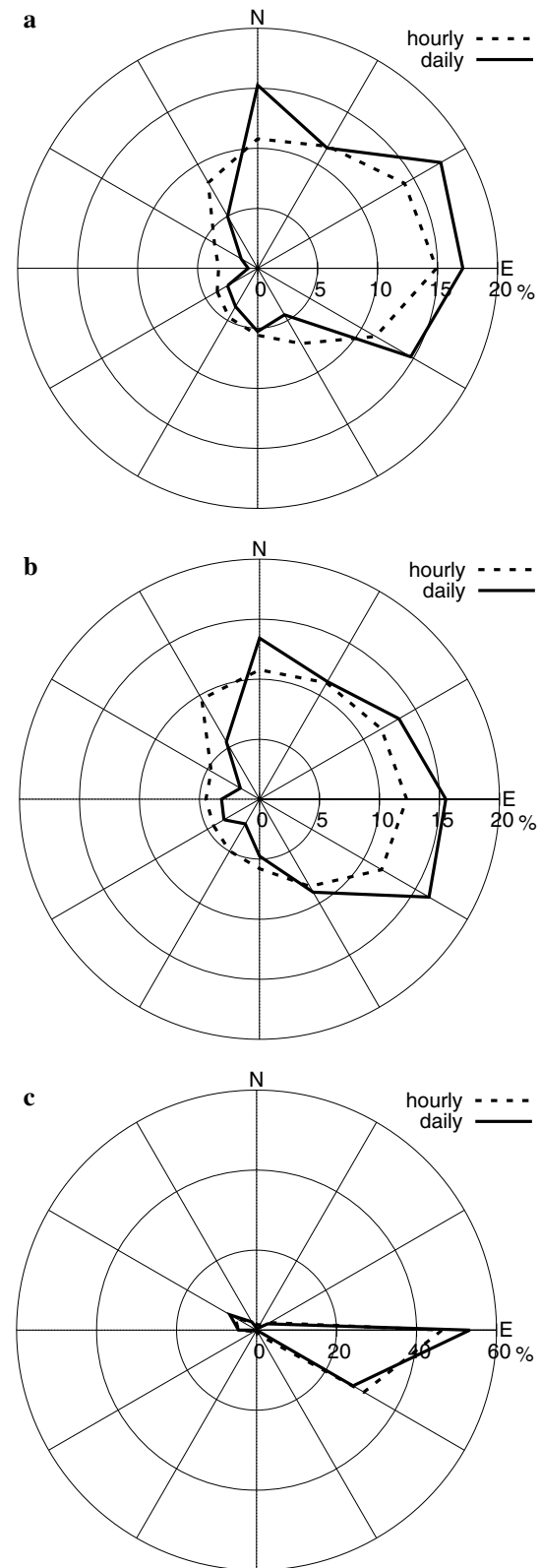
Fig. 4 Histograms of current direction at **a** ME1–3, **b** ME1–4, and **c** ME3–3. Solid lines are for daily currents and broken lines are for hourly currents. Histograms are expressed as percentages of every 30-degree bin

Fig. 5 Variances of current velocity components *u* and *v* in three period bands of T > 20, 20 > T > 2, and T < 2 days at ME1–3, ME1–4, and ME3–3
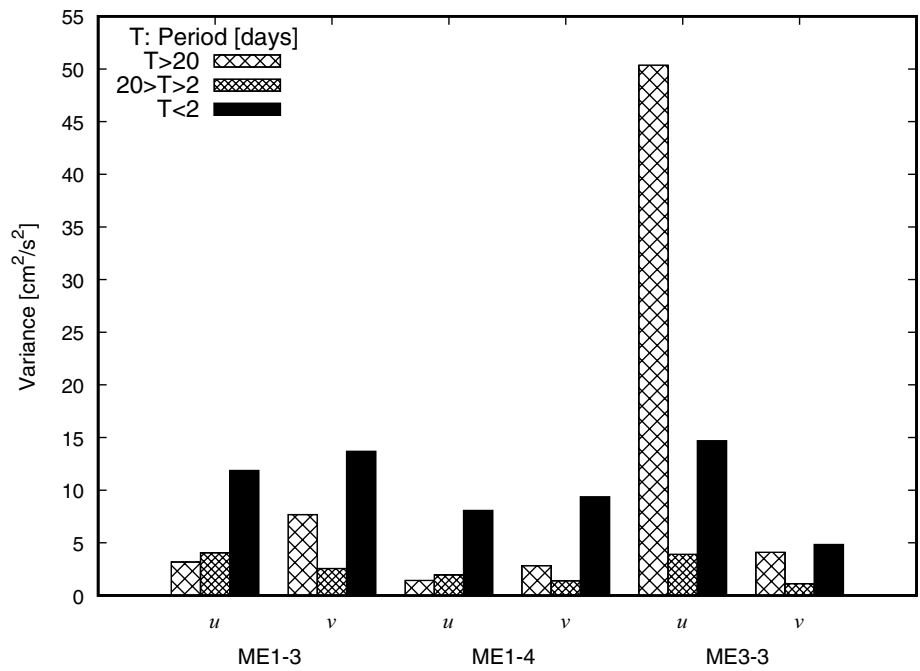

Fig. 6 LADCP currents and current-meter mean currents around the Main Gap. Blue and green arrows show vertically averaged currents by LADCP between 10-m and 50-m heights above the seafloor at the KH-16–3 and RF1206 sections, respectively. Red arrows show temporally mean currents by current meters at ME1–3 (450-m above the seafloor) and ME3–3 (40-m above the seafloor). Black arrow annotated with HT shows the mean current at a 3947-m depth at 38°58′N, 171°06′E (5070-m bottom depth according to ETOPO1) by Hamann and Taft (1987)
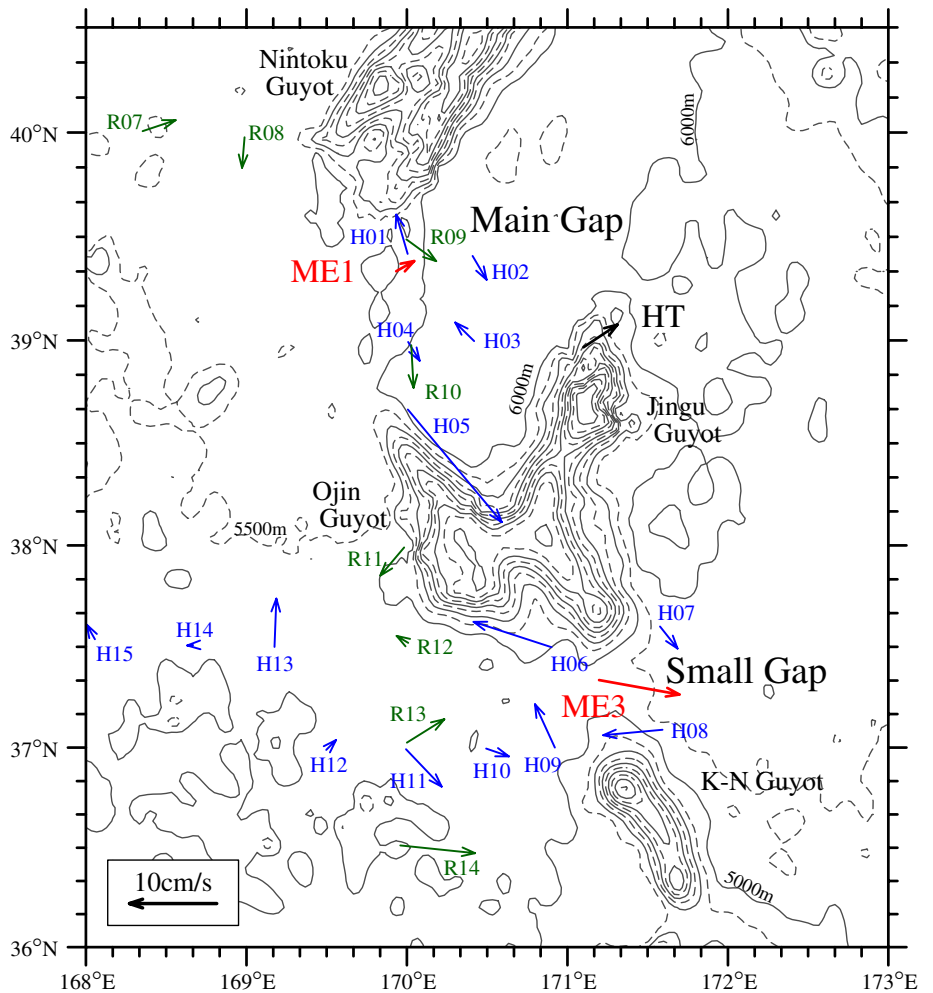
detected a westward current for about 1 month just after the deployment (Fig. 3). The westward mesoscale fluctuation at ME3 would occur within the range of H06, H08, and H09. On the other hand, eastward currents were dominant at H10–H12 and R13 to the west of the Small Gap.

Near the southern end of the Main Gap, a strong southeastward current with a velocity of 16.8 cm s^{-1} (127°T) at H05 was prominent. A northeastward mean current velocity of 4.7 cm s^{-1} (56°T) was also observed at a depth of 3947 m at the north flank of the Jingu Guyot with moorings by Hamann and Taft (1987) (shown as HT in Fig. 6). These currents flowed along the isobaths north of the tall two-peak seamount that consists of Ojin Guyot and Jingu Guyot. It is suggested that an intensified eastward flow exists on the steep northern slope of the seamount. Furthermore, there could exist a clockwise circulation around the seamount, which consists of these eastward currents on the northern slope and the westward current on the southern slope, as observed by LADCP at H06. It is actually known that several guyots of the ESC to the north of the Main Gap have individual clockwise circulations through various generation mechanisms (Wagawa et al. 2012). However, we cannot distinguish the westward current at H06 from the westward fluctuation shown at ME3 in the Small Gap. Therefore, it is difficult to conclude that a clockwise circulation exists around the two-peak seamount. Estimation of the net transport of abyssal water through the Main Gap will depend on the existence of clockwise circulation.

4 Abyssal water around the gaps

We investigated water properties around the two gaps using CTD data of KH-16–3 and RF1206 to judge what water mass was being transported by the eastward abyssal current through the gaps. In Fig. 7, vertical profiles of potential temperature (θ), practical salinity (S), and dissolved oxygen (O) are plotted, color-coded by area classification of CTD location in Fig. 2a. Abyssal water below a depth of 4000 m in the SSES region was the coldest, the most saline and the most oxygen-rich among the five regions. S exceeding 34.692 and θ below 1.07 °C near the seafloor, as shown in Fig. 7, show the characteristics of LCDW carried to the south of 37°N by the DWBC (Kawabe and Taira 1998). There was a distinct bifurcation of θ, S and O at a depth of approximately 5000 m between the SSES and the other regions. Abyssal water in the MG region had similar θ, S and O profiles to those from a depth of 4000 m to the seafloor in the NWMG region. θ–S relationships also had different curves between the SSES and MG/NWMG regions below a bifurcation point at $\theta = 1.09$ °C that existed at a depth of approximately 5000 m in the Main Gap (not shown).
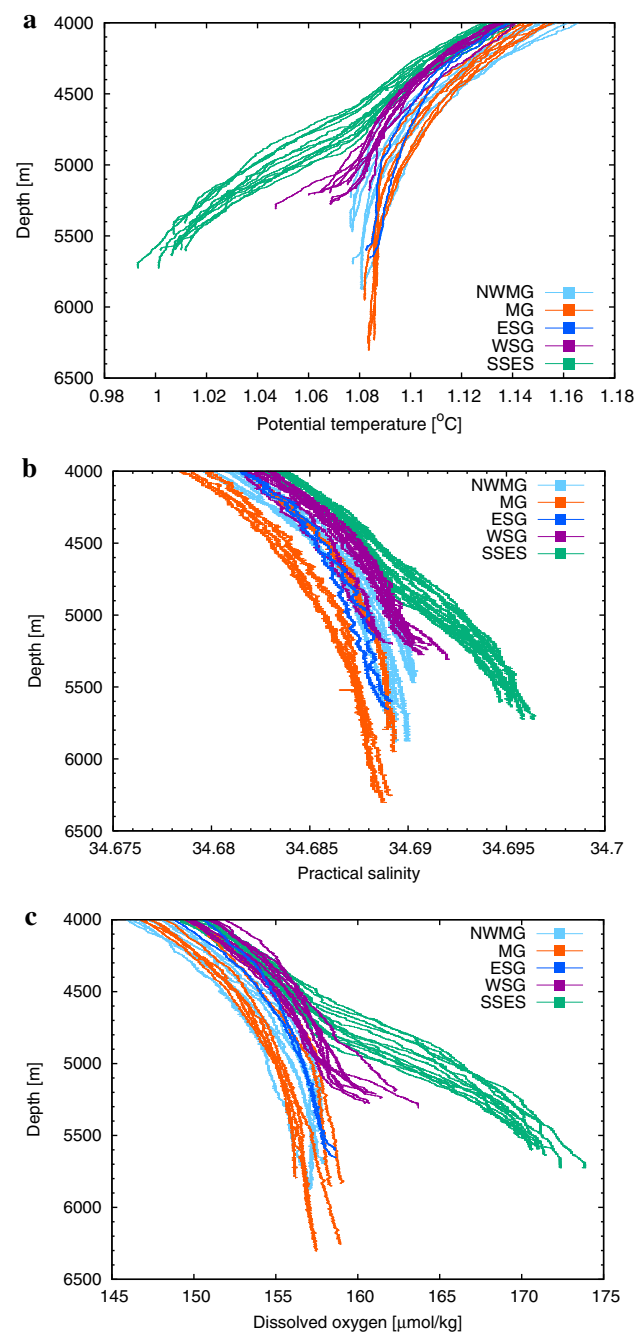

Fig. 7 Vertical profiles of **a** potential temperature, **b** salinity, and **c** dissolved oxygen observed in RF1206 and KH-16–3. Profiles in the NWMG, MG, ESG, WSG, and SSES regions (see Fig. 2b) are shown by light blue, orange, blue, purple, and green lines, respectively

To track the origin of abyssal water in the Main Gap, we plotted θ near the seafloor over a depth of 5000 m in a wider map using JMA and CCHDO data sets (Fig. 8). The bottom θ was averaged within the lowest 10 m of each CTD cast, which was lowered to approximately 10 m above the seafloor. Abyssal water in the Main Gap had θ of 1.081–1.087 °C. It was as warm as not only those at 40°N

Fig. 8 Potential temperature distribution near the seafloor with greater depths than 5000 m in the western North Pacific from 2011 to 2016. Potential temperature is colored at each station according to the color bar and is also contoured using a GMT 6 command, nearneighbor. Isobaths of a 5000-m depth are shown by thick gray lines based on ETOPO1
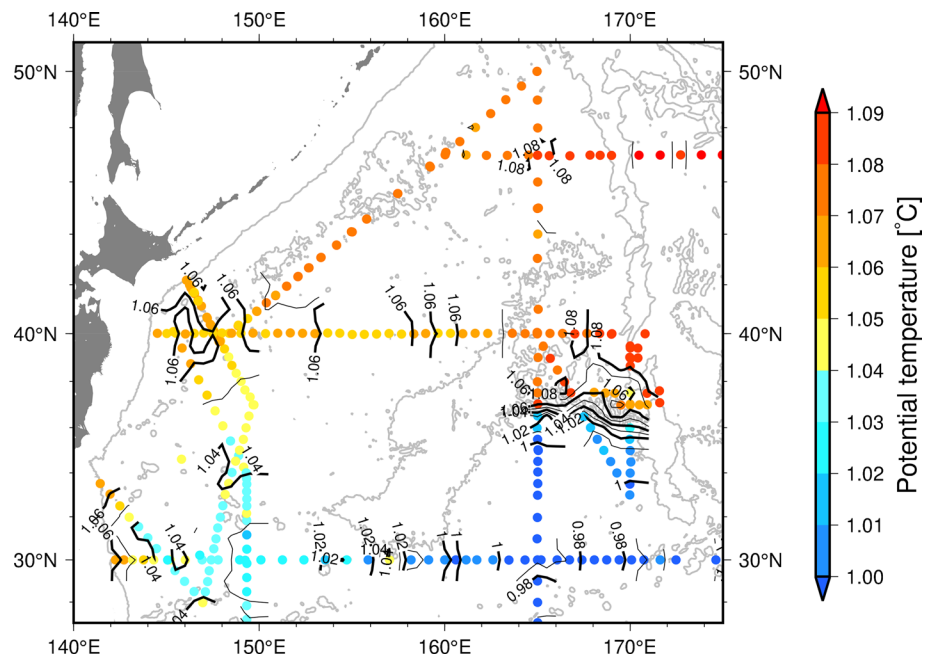
between the Shatsky Rise and the ESC but also those to the west of the ESC at 47°N, where θ was 1.080–1.083 °C. Thus, the abyssal water flowing eastward through the Main Gap is considered to originate in the northern part of the NWPB.

To the west of the Small Gap (the WSG region), abyssal water below a depth of approximately 5100 m (about 200 m above the seafloor) had θ, S and O of intermediate values between SSES and the others (Fig. 7); these θ, S and O were close to the values at a depth of approximately 5000 m in the SSES region (about 300 m above the seafloor of the WSG region). It can be inferred that this water was LCDW spilling through the S–E Seamounts from the SSES region. Furthermore, potential temperature had a spatial contrast within the WSG region in the KH-16–3 section, while the bottom θ was below 1.07 °C at the WSG stations, except for H06 and H12 (Fig. 9): H12 was a relatively shallow site. The abyssal water at H06 was presumably affected by the westward current of the clockwise circulation around the two-peak seamount or the temporary westward current in the Small Gap at the time of the KH-16–3 section. On the other hand, the abyssal water at the other WSG stations seemed to be outside the mesoscale structure of the temporary westward current in the Small Gap (Fig. 6) and was presumably less affected by it. A group of the coldest bottom waters was found at H14 and H15, and their depths were shallower than those at H09 and H10. The bottom waters at H13, H11, H10, and H09 formed a group of the second coldest waters. It is suggested that LCDW spills into the middle part of the S–E Seamounts around H14 and H15 and then spreads to the deeper portions of the WSG region, such as H09 and H10.
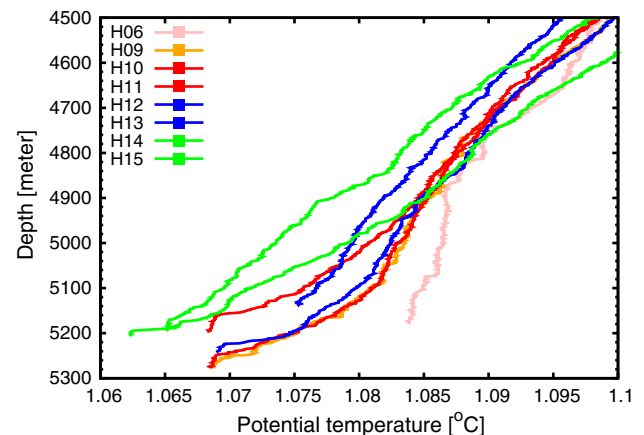

Fig. 9 Vertical profiles of potential temperature at H06–H15 in the WSG region. These are the same as the purple profiles in Fig. 7a except that only data from 2016 were used

To the east of the Small Gap (the ESG region), abyssal water lacked the low θ and high S and O characteristics shown in the WSG region and resembled those in the MG and NWMG regions (Fig. 7). The bottom waters in ESG and MG/NWMG regions were also as warm as those in the northern NWPB (Fig. 8). LCDW from the SSES region spread only over the seafloor of the WSG region and did not extend further. The temporary westward current in the Small Gap at the time of the ESG casts may have caused some anomalous water properties in the ESG region. When the abyssal current flowed eastward through the Small Gap, LCDW would possibly have been carried by the eastward current and existed in the ESG region. However, the

eastward extent of LCDW lying below a depth of 5100 m in the WSG region was believed to be mostly blocked by the sill depth of 5150–5200 m in the Small Gap (Fig. 2c). It is suggested that the strong eastward mean current at ME3 carried the warmer abyssal water, which probably came from the northern NWPB and overlay LCDW in the WSG region.

5 Estimation of volume transports of abyssal water

We obtained statistics of abyssal current at the Main Gap from the single mooring. Moreover, LADCP currents suggested that the abyssal flow on the flat portion of the Main Gap would have velocity magnitudes comparable to the mooring result. Therefore, the volume transport of the abyssal water through the Main Gap is roughly estimated as 1.6×10^6 m^3 s^{-1}, assuming a 100-km width and a 1000-m thickness below a depth of 5000 m over the seafloor at a depth of 6000 m, and an eastward current speed of 1.6 cm s^{-1} as the average of the mean u at ME1–3 and ME1–4. In this estimation, we excluded the volume transport carried by the intensified eastward current over the steep slope of the two-peak seamount south of the Main Gap, because this current would probably constitute a clockwise circulation around the two-peak seamount, as above.

We also estimate the volume transport of the abyssal water through the Small Gap roughly as 0.5×10^6 m^3 s^{-1}, assuming a 30-km width of the Small Gap and a 200-m thickness from the sill depth of 5200 m to the bifurcation depth of 5000 m between the LCDW in the SSES region and the abyssal water in the MG/NWMG regions, and 9 cm s^{-1} mean current speed at ME3–3.

6 Summary and discussion

We carried out 1-year mooring observation at the abyssal depth of the Main Gap and the Small Gap from 2016 to 2017. The abyssal current flowed slowly eastward but statistically significantly on the flat portion of the Main Gap. Its temporal current variation was dominated by tidal and inertial fluctuations. Snapshots of abyssal current observed by LADCP indicated that the currents were also very weak within the tidal and inertial variability on the flat bottom occupying most of the gap. On the other hand, at the Small Gap, the abyssal current flowed eastward at a high mean speed of 9 cm s^{-1} and had large mesoscale variability with a zonal deviation of ± 7 cm s^{-1}.

The mesoscale variability at 39°20′N in the Main Gap had only approximately one-fifth the kinetic energy of that at 37°20′N in the Small Gap. The source of the mesoscale variability is thought to be the Kuroshio Extension (KE), which

flows eastward with the current axis between approximately 32°N and 36°N at 170°E in 2016 and 2017 (Qiu et al. 2020). The abyssal mesoscale variability in the North Pacific is known to decrease meridionally with distance from the axis of the KE and to decrease eastward along the KE from a maximum at 147°E–152°E (Schmitz 1984, 1988; Miyamoto et al. 2020). At 147°E, the abyssal mesoscale variability at a depth of 4000 m is strong even at 30°N about 500 km away from the KE (Miyamoto et al. 2020), while it could decrease more rapidly with distance from the KE at 170°E. Schmitz (1988) showed that the mesoscale variability was extremely weak at a depth of 4000 m at 39°N, 175°E from 2-year mooring. The horizontal distribution and the mechanisms of the abyssal mesoscale variability around the ESC are expected to be clarified by future accumulation of current observations as well as advanced modelling based on high-resolution topographic data.

Hydrographic data analysis showed that the abyssal water flowing eastward through the Main Gap was dominated by the abyssal water coming from the northern part of the NWPB. Its volume transport was roughly estimated as 1.6×10^6 m^3 s^{-1} without counting the strong eastward current on the steep slope at the southern end of the Main Gap. This conflicts with the observation results by Komaki and Kawabe (2009) in 2003; they concluded that a part of the LCDW, which is carried to the south of the S–E Seamounts by the DWBC, crosses over the S–E Seamounts, passes the Main Gap and is transported eastward. CTD data in 2012–2016 also showed that LCDW existed to some extent near the seafloor to the north of the S–E Seamounts (WSG region). However, LCDW from the south was not dominant at the Main Gap or further north. It was not detected to the east of the Small Gap (ESG region) either. The strong eastward mean current at the Small Gap was estimated to carry the abyssal water coming from the northern NWPB, with a volume transport of 0.5×10^6 m^3 s^{-1}.

Because abyssal water is not formed in the Pacific, the abyssal water in the northern NWPB should be a remnant of LCDW, which is brought by the DWBC advancing northward east of the Japan Trench. Kawabe et al. (2009) estimated the volume transport of LCDW with $\theta < 1.2$ °C as approximately 6×10^6 m^3 s^{-1}, summing the two branches of the DWBC southwest of the Shatsky Rise, which join east of the Japan Trench (Fig. 1). Therefore, the inflow transport of LCDW into the NWPB would be 6×10^6 m^3 s^{-1}, even though a small amount of LCDW spills through the S–E Seamounts, upstream of the DWBC above the Shatsky Rise. On the other hand, the remnant of LCDW from the northern NWPB flowed out to the NEPB with a volume transport of 1.6×10^6 m^3 s^{-1} through the Main Gap and 0.5×10^6 m^3 s^{-1} through the Small Gap. The upwelling of LCDW in the NWPB is estimated as 1×10^6 m^3 s^{-1} (Kawabe and Fujio 2010). These lead to approximately 3×10^6 m^3 s^{-1} as

the outflow transport of LCDW from the NWPB along the northern route through the junction of the Kuril and Aleutian Trenches (broken line in Fig. 1). This route was only inferred from sediments (Owens and Warren 2001). Future current and water–mass observations of the northern route are expected for clarification of the volume budget of deep ocean circulation in the North Pacific.

Data Availability The data presented in this paper are available from the corresponding author upon request.

References

Ando K, Kawabe M, Yanagimoto D, Fujio S (2013) Pathway and variability of deep circulation around 40°N in the northwest Pacific Ocean. J Oceanogr 69:159–174. https://doi.org/10.1007/s10872-012-0164-2

Bower AS, Lozier MS, Gary SF, Böning CW, C. W. (2009) Interior pathways of the North Atlantic meridional overturning circulation. Nature 459:243–247. https://doi.org/10.1038/nature07979

Bower AS, Lozier MS, Gary SF (2011) Export of Labrador Sea Water from the subpolar North Atlantic: A Lagrangian perspective. Deep Sea Res Part II 58:1798–1818. https://doi.org/10.1016/j.dsr2.2010.10.060

Dickson RR, Gould WJ, Muller TJ, Maillard C (1985) Estimates of the mean circulation in the deep (>2000m) layer of the eastern North Atlantic. Prog Oceanogr 14:103–127. https://doi.org/10.1016/0079-6611(85)90008-4

Fujio S, Yanagimoto D (2005) Deep current measurements at 38°N east of Japan. J Geophys Res. https://doi.org/10.1029/2004jc002288

Hamann I, Taft BA (1987) On the kuroshio extension near the emperor seamounts. J Geophys Res 92(C4):3827. https://doi.org/10.1029/jc092ic04p03827

Johnson GC, Toole JM (1993) Flow of deep and bottom waters in the Pacific at 10°N. Deep Sea Res Part I 40(2):371–394. https://doi.org/10.1016/0967-0637(93)90009-r

Kato F, Kawabe M (2009) Volume transport and distribution of deep circulation at 165°W in the North Pacific. Deep Sea Res Part I 56(12):2077–2087. https://doi.org/10.1016/j.dsr.2009.08.004

Kawabe M, Fujio S (2010) Pacific ocean circulation based on observation. J Oceanogr 66(3):389–403. https://doi.org/10.1007/s10872-010-0034-8

Kawabe M, Taira K (1998) Water masses and properties at 165°E in the western Pacific. J Geophys Res 103(C6):12941–12958. https://doi.org/10.1029/97JC03197

Kawabe M, Fujio S, Yanagimoto D (2003) Deep-water circulation at low latitudes in the western North Pacific. Deep Sea Res Part I 50(5):631–656. https://doi.org/10.1016/s0967-0637(03)00040-2

Kawabe M, Yanagimoto D, Kitagawa S, Kuroda Y (2005) Variations of the deep western boundary current in Wake Island Passage. Deep Sea Res Part I 52(7):1121–1137. https://doi.org/10.1016/j.dsr.2004.12.009

Kawabe M, Fujio S, Yanagimoto D, Tanaka K (2009) Water masses and currents of deep circulation southwest of the Shatsky Rise in the western North Pacific. Deep Sea Res Part I 56(10):1675–1687. https://doi.org/10.1016/j.dsr.2009.06.003

Komaki K, Kawabe M (2009) Deep-circulation current through the Main Gap of the Emperor Seamounts Chain in the North Pacific. Deep Sea Res Part I 56(3):305–313. https://doi.org/10.1016/j.dsr.2008.10.006

Mantyla AW, Reid JL (1983) Abyssal characteristics of the World Ocean waters. Deep Sea Res Part A Oceanograp Res Papers 30(8):805–833. https://doi.org/10.1016/0198-0149(83)90002-x

Miyamoto M, Oka E, Yanagimoto D, Fujio S, Mizuta G, Imawaki S, Kurogi M, Hasumi H (2017) Characteristics and mechanism of deep mesoscale variability south of the Kuroshio Extension. Deep Sea Res Part I 123:110–117. https://doi.org/10.1016/j.dsr.2017.04.003

Miyamoto M, Oka E, Yanagimoto D, Fujio S, Nagasawa M, Mizuta G, Imawaki S, Kurogi M, Hasumi H (2020) Topographic rossby waves at two different periods in the northwest pacific basin. J Phys Oceanogr 50(11):3123–3139. https://doi.org/10.1175/JPO-D-19-0314.1

Oka E, Kouketsu S, Yanagimoto D, Ito D, Kawai Y, Sugimoto S, Qiu B (2020) Formation of Central Mode Water based on two zonal hydrographic sections in spring 2013 and 2016. J Oceanogr 76(5):373–388. https://doi.org/10.1007/s10872-020-00551-9

Owens W, Warren BA (2001) Deep circulation in the northwest corner of the Pacific Ocean. Deep Sea Res Part I 48(4):959–993. https://doi.org/10.1016/s0967-0637(00)00076-5

Qiu B, Chen S, Schneider N, Oka E, Sugimoto S (2020) On the reset of the wind-forced decadal kuroshio extension variability in late 2017. J Clim 33(24):10813–10828. https://doi.org/10.1175/JCLI-D-20-0237.1

Richardson PL (2008) On the history of meridional overturning circulation schematic diagrams. Prog Oceanogr 76(4):466–486. https://doi.org/10.1016/j.pocean.2008.01.005

Roden GI, Taft BA, Ebbesmeyer CC (1982) Oceanographic aspects of the emperor seamounts region. J Geophys Res 87(C12):9537–9552. https://doi.org/10.1029/JC087iC12p09537

Rudnick DL (1997) Direct velocity measurements in the Samoan Passage. J Geophys Res Oceans 102(C2):3293–3302. https://doi.org/10.1029/96jc03286

Schmitz WJ (1984) Abyssal Eddy kinetic energy levels in the western north pacific. J Phys Oceanograp 14(1):198–201. https://doi.org/10.1175/1520-0485(1984)014%3C0198:AEKELI%3E2.0.CO;2

Schmitz WJ (1988) Exploration of the eddy field in the midlatitude North Pacific. J Phys Oceanogr 18(3):459–468. https://doi.org/10.1175/1520-0485(1988)018%3C0459:EOTEFI%3E2.0.CO;2

Thompson RORY (1983) Low-pass filters to suppress inertial and tidal frequencies. J Phys Oceanogr 13(6):1077–1083. https://doi.org/10.1175/1520-0485(1983)013%3C1077:LPFTSI%3E2.0.CO;2

Uchida H, Kawano T, Nakano T, Wakita M, Tanaka T, Tanihara S (2020) An Expanded batch-to-batch correction for IAPSO standard seawater. J Atmos Oceanic Tech 37(8):1507–1520. https://doi.org/10.1175/JTECH-D-19-0184.1

Wagawa T, Yoshikawa Y, Isoda Y, Oka E, Uehara K, Nakano T, Kuma K, Takagi S (2012) Flow fields around the Emperor Seamounts detected from current data. J Geophys Res Oceans 117(C6):C06006. https://doi.org/10.1029/2011JC007530

Yanagimoto D, Kawabe M (2007) Deep-circulation flow at mid-latitude in the western North Pacific. Deep Sea Res Part I 54(12):2067–2081. https://doi.org/10.1016/j.dsr.2007.09.004

Yanagimoto D, Kawabe M, Fujio S (2010) Direct velocity measurements of deep circulation southwest of the Shatsky Rise in the western North Pacific. Deep Sea Res Part I 57(3):328–337. https://doi.org/10.1016/j.dsr.2009.12.004